Coseismic surface deformation, fault modeling and Coulomb stress changes of the March 2021 Thessaly, Greece, earthquake sequence based on InSAR and GPS data

Charalampos (Haris) Kontoes[1], Stavroula Alatza[1], Konstantinos Chousianitis[2], Nikos Svigkas[3], Constantinos Loupasakis[4], Simone Atzori[3], Alexis Apostolakis[1]

[1] Institute for Astronomy, Astrophysics, Space Applications and Remote Sensing, Center for Earth Observation Research and Satellite Remote Sensing BEYOND, National Observatory of Athens, Metaxa & Vas. Pavlou, 15236, Athens, Greece

[2] Institute of Geodynamics, National Observatory of Athens, Lofos Nymfon, 11810, Athens, Greece

[3] Instituto Nazionale di Geofisica e Vulcanologia, 00143 Rome, Italy

[4] Laboratory of Engineering Geology and Hydrogeology, Department of Geological Sciences, School of Mining and Metallurgical Engineering, National Technical University of Athens, 15780 Athens, Greece

Corresponding author: **Charalampos (Haris) Kontoes** (kontoes@noa.gr), Tel: +30 2103490011,

Address: Institute for Astronomy, Astrophysics, Space Applications and Remote Sensing, Center for Earth Observation Research and Satellite Remote Sensing BEYOND, National Observatory of Athens, Metaxa & Vas. Pavlou, 15236, Athens, Greece

Declaration of Competing Interests

The authors acknowledge there are no conflicts of interest recorded.

Abstract

In March 2021 three strong earthquakes with magnitudes (M_w) of 6.3, 6.0 and 5.2 occurred in Thessaly plain, Greece, on 3, 4 and 12 March, respectively. The modeling of all three sources, by inversion of InSAR and GPS data, indicates a NE–SW trending extensional stress field with indications for NE dipping sources. The unmapped fault source of the first mainshock (M_w 6.3) is located approximately 6 km to the SW of the known Larissa Fault. Moreover, the fault that was activated during the second mainshock (M_w 6.0), appears to be located more to the north, bordering the Titarisios river valley to the SW, while the third mainshock (M_w 5.2), appears to be triggered at a fault segment located further to the NW. The Coulomb stress analysis using the slip distributions of the three aforementioned mainshocks, revealed a unilateral triggering of the second and third event towards the NW and explained the spatial development of the entire aftershock sequence. Furthermore, among the already known active faults in the broader area, only the Larissa fault was brought closer to failure as a result of the imparted stress changes.

Introduction

On 3, and 4 March 2021, the northern part of the East Thessaly plain, Central Greece, was struck by two earthquakes with moment magnitudes of M_w 6.3 and M_w 6.0, respectively (Figure 1a). According to the solutions provided by the Institute of Geodynamics of the National Observatory of Athens (NOA), the first event (10:16:08 GMT) was located at 39.75°N, 22.20°W at a depth of 8 km. The second event (18:38:19 GMT) was located at 39.80°N, 22.13°W, approximately 8 km to the NW of the first earthquake, at a depth of 7 km (Figure 1a). During the 10 following days, over 600 aftershocks were recorded in the vicinity of these two sources. Among them, 87 events had a moment magnitude greater than M_w 3.5. Moreover, on 12 March 2021 (12:57:50 GMT), a third event with moment magnitude of M_w 5.2 took place towards NNW, nearby the NW edge of the Titarisios river basin, at 39.84°N, 22.01°W and at a depth of 7 km (Figure 1a).

All three major seismic events were strongly felt in more than half of Greece and attracted the attention of the majority of seismological institutes in Europe. They caused extensive damage throughout the villages of the surrounding area, namely Damasi, Vlachogianni, Mesochori and Magoula (Figure 1a), along the Titarisios valley at the north of Larissa City (Figure 1a). Approximately 600 private buildings were severely damaged beyond repair, among which churches and schools, mainly belonging to load-bearing masonry walls constructions. Luckily just a few injuries and no casualties were reported.

Moreover, significant earthquake-induced coseismic phenomena including extensive liquefaction, ground cracks and rock falls, were reported in the affected area. In particular, according to Valkaniotis et al. (2021), Koukouvelas et al. (2021), Chatzipetros et al. (2021) and Ganas et al. (2021), the earthquakes resulted in more than 400 liquefaction-related features being identified in alluvial deposits, including sand blows and craters, fissures and lateral spreading ruptures along the river banks of the Pinios and Titarisios rivers crossing the narrow strong motion site.

The study of the seismic activity required a thorough seismotectonic regime analysis of the wider Thessaly plain. As reported in the extensive literature, the tectonic structure of the wider plain is the result of three deformational phases that took place since the late Alpine Orogeny of Greece (Caputo and Pavlides, 1993; Chatzipetros et al., 2018). The oldest identified phase is a compressional ENE-WSW trending phase that has been defined as late Alpide. Following the postorogenic collapse of the External Hellenides, during the Late Miocene–Early Pleistocene, an extensional field of NE–SW was developed. The extensional forces generated a system of basins and ranges bordered by NW–SE trending normal faults (Caputo, 1990). Actually, the 60 km long, Larissa lowlands (northern part of East Thessaly plain), trending to the same direction, was formed during that event. The latter deformational phase started during the Middle to Late Pleistocene, generating faults trending E–W to ESE–WNW. Evaluating the recent seismicity records this stress field is considered as still active (Sboras et al., 2014; Caputo et al., 2012; Sboras, 2011; Papazachos and Papazachou, 1997; Ambraseys and Jackson, 1990), while geodetic extension rates have been found to be on the order of 50 ns/yr (Chousianitis et al., 2015; D'Agostino et al., 2020; Lazos et al., 2021).

Located at the northern part of the East Thessaly plain, Tyrnavos Sub – basin is bordered to the north by the ESE–WNW trending and north-dipping Tyrnavos (TF) and Larissa (LF), faults (Caputo et al., 1994). These faults mainly affect the Triassic crystalline limestone and Paleozoic mica schist and gneiss (Kilias et al., 1991; Kilias and Mountrakis, 1987) of the Pelagonian bedrock, as well as Pliocene and Quaternary deposits (Caputo, 1990).

The examined seismic sequence occurred to the NW of the previously mapped Tyrnavos (TF) and Larissa (LF) faults (Figure 1a) (Valkaniotis et al., 2021; Koukouvelas et al., 2021; Papadopoulos et al., 2021; De Novellis et al., 2021 and Ganas et al., 2021). As expected, the shallow depth of the events resulted in significant surface deformation patterns, which were revealed by satellite observations and GPS geodetic measurements. InSAR calculations and GPS data were employed to measure the surface deformation caused by the earthquake sequence, and jointly inverted to model the source properties. Finally, the potential seismic source interactions were investigated by means of Coulomb stress changes estimation.

Co-Seismic Surface Deformation

DInSAR Calculated Displacements

SAR interferometry has long been identified as an efficient tool for capturing coseismic displacements (e.g., Massonnet and Feigl, 1993; Sykioti et al., 2003) and has significantly contributed to the definition of the active faults in the Greek territory (e.g., Merryman Boncori et al., 2014; Papadopoulos et al., 2019; Svigkas et al., 2019, Papadopoulos et al., 2017). InSAR analysis of the 2021 Thessaly earthquake sequence, was performed by invoking the processing chain developed in the Center for EO Research and Satellite Remote Sensing BEYOND of NOA, so-called geObservatory (http://geobservatory.beyond-eocenter.eu/) (Papoutsis et al., 2020). geObservatory is an automatic system that creates interferograms, with the use of ENVI – SARscape, in areas affected by geohazards (earthquake, volcano eruption, etc.). When a geological hazard occurs, the service is automatically activated and ingests all available Sentinel-1 SAR data, covering the affected area, from Copernicus Data Access Hubs (ESA) and the Hellenic Mirror Site (https://sentinels.space.noa.gr/). As soon as the first seismic event in Thessaly plain was recorded, geObservatory ingested Sentinel-1 images of both ascending and descending satellite tracks (Figure 1b) and delivered co-seismic interferograms. To reduce phase noise and to improve phase unwrapping, the Goldstein and Werner (1998) adaptive filtering was implemented. The Minimum Cost Flow (MCF) approach (Constantini, 1998), was used for phase unwrapping. All the unwrapped interferograms were corrected from the topography effect using an SRTM-v4 Digital Elevation Model (Farr and Kobrick, 2000). The co-seismic deformation pattern of each of the three earthquakes individually (3, 4 and 12 March, 2021), as well as combinations of them is presented in Figure 2. Table S1 summarizes the interferometric pairs that were automatically generated by the geObservatory service, during the lasting period of the Thessaly earthquake sequence (Figure 2d).

GPS Calculated Displacements

Low-rate (30 s) data from four near-field GPS stations (Figure 1c) belonging to the NOANET network of the National Observatory of Athens (Ganas et al., 2008; Chousianitis et al., 2021), the HermesNET of the Aristotle University of Thessaloniki (Fotiou et al., 2010) and the HxGN SmartNet network of the private company Metrica S.A., were also processed. By analyzing daily observations using GAMIT/GLOBK software v10.71 (Herring et al., 2018) and following the processing approach described by Chousianitis et al. (2016) and Chousianitis and Konca (2019), position time series in the IGb14 reference frame were calculated (Figure 3). The static GPS daily solutions captured both the coseismic offsets of the M_w 6.3 and the M_w 6.0 earthquakes. To estimate static offsets, time series over 10 days prior to the first (M_w 6.3), and 8 days after the second earthquake (M_w 6.0) were averaged. Next the differences between each of these average positions were calculated with the position that was derived for the time interval between the first and the second mainshock (i.e., from 3 March 2021 at 10:16:08 until 4 March 2021 at 18:38:19). The latter was achieved by cutting the corresponding RINEX files of 3 and 4 March, so as to include only data after the M_w 6.3 and before the M_w 6.0 earthquake. The calculated coseismic offsets along with their associated uncertainties, are reported in Table 1. As expected for a normal event which occurred on a NW-SE rupture plane, the GPS stations which are located to the south (foot wall) had horizontal static offsets towards the SW direction, while those located to the north (hanging wall), towards the NE direction.

Geodetic data modeling

Source modeling is based on a consolidated scheme with a non-linear inversion to define the geometry of the sources and the mechanism of the rupture, followed by the estimation of slip distribution, using a linear inversion (Wright et al., 2003); in both cases, the equations for a dislocation in an elastic half-space medium (Okada, 1985) and the optimization procedures are described in Atzori et al. (2009) and Atzori et al. (2019). The inversion is carried out with a set of points sampled from the raster displacement maps and includes, in all cases, GPS coseismic offsets described in the previous paragraph. Posting of input datasets was performed with double resolution, finer the area of higher displacements and coarser far from the near field. Details about sampling areas, posting resolutions and number of points inverted for every dataset can be found in the Supplemental material, while the rationale behind this approach is explained in Atzori and Antonioli (2011).

The modeling of the three events considered in this work followed a complex sequence of non-linear and linear inversion, to fully exploit the availability of InSAR pairs containing the isolated and the joint displacement fields of the first and second events. In synthesis, the availability of InSAR pairs isolating first and second events (Feb. 25 - Mar. 3 and Mar. 3 - Mar. 9, ascending orbit), allowed for separated non-linear inversions of the two events, then refined in a joint non-linear inversion with both sources and both orbits (Feb. 25 – Mar. 9 from ascending orbit and Mar.

2 – Mar. 8 from descending orbit). The third, M_w 5.2, event was then modeled independently with the ascending and descending pairs acquired in the same days (Mar. 8 – Mar. 14). A complete description of the inversions to derive the source geometry and rupture mechanisms can be found in the Supplemental Material.

After the definition of the two uniform-slip sources, the linear inversion was conducted to get the slip distributions, with a non-negative least-square algorithm and allowing, only for the first two events, a small rake variability of 15° from the average value of the non-linear inversion. The slip distribution was calculated for patches of size 1x1 km. An orbital ramp was also modeled and removed, when jointly inverting ascending and descending InSAR data. In both non-linear and linear inversions, a topographic compensation was adopted (Williams and Wadge, 1998) and an automatic weighting of datasets was performed according to the approach described in Atzori et al. (2019). The reliability of the constrained sources is witnessed with the comparison between the observed and predicted InSAR data, shown with the residuals in Figures 4 and 5.

One goal of modeling is the discrimination between real and auxiliary planes that possibly generated the three earthquakes; nearly all the parameters where left free to vary, in intervals large enough to include both planes (Table 2). This was not required for the first event, because the fringe distribution shows higher spatial frequency on the western side (Figure 2a), a consequence of the fault top at West of the displacement pattern, with North-East dipping direction. The estimated values for strike, dip and rake are 312°, 39° and -90°, respectively, with a uniform slip source of releasing a moment magnitude of $2.93 \cdot 10^{18}$ N·m, corresponding to a M 6.27 earthquake, in perfect agreement with M_w 6.3. Results are in a general accordance to both the moment tensor solutions of the Aristotle University of Thessaloniki (AUTH) (Strike/Dip/Rake=314°/36°/-88°) (Karakostas et al., 2021) and that of the National Observatory of Athens (NOA) (Strike/Dip/Rake=323°/33°/-74°) (https://bbnet.gein.noa.gr/HL/seismicity/mts). The M_w 6.0 event, instead, can be equally modeled by means of a NE-dipping or a SW-dipping fault plane. However, as in the case of the first seismic event, the epicenter is located East of the deformation pattern, i.e. at the bottom of the rupture(Figure 2b): this was observed in several earthquakes with normal mechanism, like Athens 1999 (Atzori et al., 2008), L'Aquila 2009 (Atzori et al., 2009), Amatrice and Norcia 2016 (Cheloni et al., 2017), suggesting a rupture starting at bottom and propagating upward along the fault; this option is also the more realistic to make the fault plane compatible with the hypocenter positions. The retrieved parameters for this event are strike 289°, dip 43° and rake -107°, for an event of moment magnitude of 7.4·1017 N·m, corresponding to M 5.88. More difficult is the case of the M_w 5.2 event, where both planes equally predict the displacement and the fringe shape giving only a small preference for the antithetic, i.e. SW dipping, solution. This option, however, would contradict the similarity of the three ruptures, being also in this case the epicenter East of the deformed area. Therefore, both solutions are presented, suggesting that the NE dipping plane (strike/dip/rake of 286°/29°/-87°) is slightly preferred to the antithetic, SW dipping, hypothesis (strike/dip/rake of 106°/54°/-87°); both uniform slip solutions correspond to an event of magnitude 5.5. Here we note that although relocated seismicity (Ganas et al. 2021; Kassaras et al. 2022) confirms the NE-dipping planes of the first two mainshocks, it is incapable of distinguishing between a NE- or a SW-dipping surface. The main parameters of the three segments are reported in Table 2, with their 1-σ uncertainty: all the events show nearly pure normal mechanisms, in line with the already published fault plane solutions.

It is likely that the two events occurred on adjacent segments of the same fault (Figure 6), however we cannot rule out the possibility to have had an activation of distinct faults of the area. The sources have the same depth of the slip peaks at about 5.5 km, while the dislocated area and the maximum values reflect the different release of seismic moment, as shown with the slip distributions in Figure 7. Local residuals are still present: they can be attributed to deformations after ground liquefaction or local fluctuations from the planar elastic model. We don't exclude that a fraction of residuals could be ascribed to post-seismic deformation that occurred in the volume around the source.

The solution reliability can be checked with the comparison of the observed vs. modeled data, with the residuals in Figures 4 and 5 and Table 3. For sake of completeness, the point shapefiles containing the linear inversion results are provided in the "insar_data.zip" file in the Supplemental material (see the readme.txt file with the explanation of alphanumeric attributes).

Coulomb Stress Transfer and Earthquake Triggering

Using the slip distributions of the three mainshocks of M_w 6.3, M_w 6.0 and M_w 5.2 and the Coulomb 3.4 software (Lin and Stein, 2004; Toda et al., 2005), the corresponding Coulomb stress changes were calculated. For all calculations a 0.25 Poisson's ratio, a shear modulus of 32 GPa, and a coefficient of friction of 0.4, were selected. Values which are commonly used in Coulomb stress calculations associated with continental faults (Harris 1998; Parsons et al. 1999; Hodge et al. 2018). Stress changes were resolved on optimally oriented normal faults, since the broader epicentral area is a well-known extensional domain. In this context, a regional tensional tectonic stress of 100 bars was adopted with the maximum stress axes plunge at vertical angles and minimum stress axes horizontal towards a NNW-SSE direction (Kapetanidis and Kassaras, 2019). The coseismic Coulomb stress changes as a result of the M_w 6.3 earthquake of 3 March are depicted in Figure 8a, where we have superimposed only the aftershocks which occurred between the origin time of this event and until the occurrence of the second earthquake (M_w 6.0) on 4 March. It is evident from Figure 8a that the location of the second event of M_w 6.0 (green star) was brought closer to failure and the calculated zones of Coulomb stress increase are well-correlated with the aftershocks that had occurred until that time. Next, in Figure 8b we present the stress changes induced by the M_w 6.3 and the M_w 6.0 ruptures and the superimposed seismicity corresponds to the aftershock sequence until the occurrence of the third event of M_w 5.2 (green star) on 12 March. The combined Coulomb stress changes caused by the M_w 6.3 and M_w 6.0 earthquakes highlight that after the occurrence of the M_w 6.0 event, the seismic sequence started to develop towards the NW, through an area where no aftershocks had occurred until that time (see black circle in Figure 8a). It is also evident that the site of the third earthquake was brought closer to failure by the previous large earthquakes of 3 and 4 March. Finally, in Figure 8c we show the variation of Coulomb stress caused by all three seismic events (M_w 6.3, 6.0 and 5.2) and we superimposed the seismicity after the origin time of the M_w 5.2 earthquake and until November 2021. The calculations in Figure 8c have been performed using the slip distribution of the NE dipping fault plane for the M_w 5.2 event, although an almost identical pattern has been derived using the SW dipping fault plane as well. In this panel it is illustrated that after the occurrence of the M_w 5.2 earthquake and especially for the depth range from 4 km to 12 km, the calculated stress increases contributed to the development of the aftershock sequence once again towards the NW, through an area which exhibited limited seismic activity until then (see circle in Figure 8b). Thus, the Coulomb stress analysis revealed that the M_w 6.3 rupture triggered the M_w 6.0 earthquake of 4 March and this event subsequently triggered the M_w 5.2 earthquake of 12 March and completely explained the distribution and the unilateral spatial development of the aftershock sequence towards the NW direction.

Following, we evaluated the possible effects of the Thessaly plain seismic sequence on the mapped active faults in the area, namely the Larissa, Tyrnavos and Rodia faults. To do so, we used the slip distributions of the three mainshocks and estimated the Coulomb stress imparted to these individual "receiver" fault planes which were modeled as 60° dipping pure normal faults (i.e. assuming a slip direction of -90°). To assess the variations of Coulomb stress across the three fault planes, we divided them into patches. The results are illustrated in Figure 9, where it is revealed that the largest part of the Larissa fault was brought significantly closer to failure since it was loaded by more than 0.2 bars of stress. This implies increased seismic risk, although the low slip rate (< 0.2 mm/yr) of this structure as evidenced by paleoseismological studies (Caputo et al., 2004, 2006) points to a long recurrence interval. Contrary to the Larissa fault, failure was not promoted to the Tyrnavos and Rodia faults since their rupture planes received stress decreases.

Discussion

As indicated by the interferograms and the geodetic data modeling all three major events occurred on adjacent NW–SE trending normal faults, developed in agreement with a NE–SW trending extensional stress field. The fault plane solutions and the spatial distribution of the aftershocks confirm the activation of structures of such orientation, which deviate from the typical E-W trending of the presently active faults of Thessaly.

The main M_w 6.3 event, striking 312° (F1 in Figure 2e), occurred along a synthetic fault plane to the Larissa Fault (LF), identified approximately 6 km to the SW of LF. The dip angle of the activated fault was estimated at 39.6° (±4.6°) to the NE. As indicated by the geodetic data modeling, the dislocated area extends for 11.2 to 9.4 km with an average slip of 0.9 m and a peak slip of about 1.2 m. Based solely on the model, the slip barely reaches the surface. This is an unknown and unmapped fault and according to Pavlides et al. (2021) even after its current activation no clear morphogenic deformation signs can be identified along the surface.

The fault segment which was activated during the second M_w 6.0 event (F2, Figure 2e) is located to the NW of the first event with a strike of 289.5° (±7.3°), bordering the Titarisios river valley to the SW. Considering the scenario of the activation of distinct faults at the area, if the second event occurred on a different fault than that of the first event, it has a good alignment with the extension of the Larissa fault (LF) to the NW. The dip angle of this fault was estimated at 43.1° (±9.3°) to the NE, with an average slip of 0.5 m. This was also an unknown fault, never mapped before. According to Koukouvelas et al., (2021) the visible traces of this fault were extending for more than 10 km, crossing the recent alluvial deposits of the Titarisios Valley. This fault segment has been named as “Vlachogianni Fault”, giving it the name of the village that was most affected by this event.

The third earthquake of 12 March 2021 appeared to have occurred at a segment extending further to the NW with a strike of 286.5°. Unlikely in that case both synthetic and antithetic planes equally predict the displacement identified by the geodetic data. However, considering the current extensional stress field, the dip direction of the surrounding major fault lines and the position of the event's epicenter with respect to the deformation field, the NE dipping appears to be more favorable. At the same time, the fringe shape gives a small preference for the antithetic plane. These remarks raise questions, which cannot be addressed by this study, since field work seems to be necessary to gain insight on this matter. In any case, both best-fit models predict an average dislocation of about 0.5 m.

As regards already published studies, Chatzipetros et al. (2021), De Novellis et al. (2021), Galanakis et al. (2021), Pavlides and Sboras (2021) Karakostas et al. (2021), have also identified two distinct segments, dipping NE, of a previously unknown fault system, that acted as a hidden or blind fault, during the M_w 6.3 and M_w 6.0 earthquake events. Actually, the only research team that diverged was that of Papadopoulos et al. (2021) which suggested that the 4 March rupture propagated further NW in an antithetic fault segment dipping SW.

Regarding the 12 March M_w 5.2 event, De Novellis et al. (2021), Ganas et al. (2021), Kassaras et al. (2022) and Papadopoulos et al. (2021), attributed this earthquake to a E-W trending, S to SW-dipping fault. Nevertheless, Ganas et al. (2021) and Kassaras et al. (2022) noted that the geometry of this fault could not be sufficiently constrained by the relocated hypocenters and that it is possible that another E-W trending but N-dipping fault was triggered within that activated volume.

Coulomb stress changes resolved on optimally oriented normal faults, illustrated that the M_w 6.3 mainshock rupture increased Coulomb stresses on the nucleation location of the M_w 6.0 event of 4 March 2021 and subsequently, the rupture of this event increased Coulomb stresses on the nucleation location of the M_w 5.2 event of 12 March 2021. The results show that the spatial distribution of the aftershocks that occurred after the M_w 6.3 event and prior to the occurrence of the M_w 6.0 event is well-correlated with the Coulomb stress-increased regions. After the occurrence of the second event of M_w 6.0, the aftershock sequence started to expand further to the NW due to increase in Coulomb stress along this direction, which was caused by the M_w 6.0 rupture. At that area, the M_w 5.2 event occurred on 12 March 2021 demonstrating the unilateral triggering towards the NW and the high correlation of the spatial development of aftershocks with the calculated stress increases at any stage during the evolution of the examined seismic sequence (Figure 8 and Figure S5). Such consistency of the spatial development of aftershocks with the areas that received positive Coulomb stress changes has been observed in other normal-faulting earthquakes in Greece including the 2017 Lesvos (Chousianitis and Konca 2018), the 2017 Bodrum-Kos (Ganas et al. 2019; Konca et al. 2019; Sboras et al. 2020) and the 2020 Samos earthquake (Chousianitis and Konca 2021; Karakostas et al. 2021; Kiratzi et al. 2021). Furthermore, among the mapped active faults in the vicinity of the Thessaly plain seismic sequence, the Larissa fault was brought significantly closer to failure, while the Tyrnavos and Rodia faults received stress decreases.

Conclusions

The Thessaly plain earthquake sequence of March 2021 has been investigated within this paper. InSAR and GPS data were exploited to measure surface deformation and model the seismic sources. Thanks to Sentinel-1 frequent acquisitions, it was possible to isolate each one of the three strong events that occurred. The geodetic modeling results indicate that the sequence was caused by previously unknown and unmapped tectonic structures that deviate from the typical E-W direction of the active faults of Thessaly. Based on the field investigations, among the activated structures only the so-called Vlachogianni fault segment provided clear evidence of morphogenic deformation along the surface. The rest of the segments could have acted as blind faults or no clear in-situ evidence of morphotectonic deformation had been identified so far. The static Coulomb stress changes caused by the three ruptures indicated that they raised the stress to the NW, activating gradually fault segments towards that direction. The imparted stress due to the three mainshocks loaded the nearby active Larissa fault and brought it closer to failure.

Data and Resources

GPS data were provided by the NOANET network of the National Observatory of Athens (http://geodesy.gein.noa.gr:8000/nginfo/), the HxGN SmartNet/Metrica S.A. network (https://www.metrica.gr/services/hxgn-smartnet-gr/info) and the HermesNET/AUTH (https://users.auth.gr/users/3/7/050473/public_html/Stations.html). InSAR and GPS data were modeled with SARscape® (sarmap, CH). Sentinel-1 data were provided by the Hellenic Mirror Site and the Sentinel Greek Copernicus Data Hubs (https://sentinels.space.noa.gr/). The BEYOND geObservatory (http://geobservatory.beyond-eocenter.eu/) processing chain, was used for the generation of the co-seismic interferograms. Information about Sentinel-1 co-seismic interferograms is added in the Supplemental material. Maximum Coulomb stress changes are also presented with the seismic events (M_L>2.0; 3 March - 30 November) superimposed. A detailed description of the strategy adopted to model the source of the three seismic events is also provided in the Supplemental material, along with an “insar_data.zip” file, with the shapefiles of InSAR data from the final linear inversion.

Acknowledgments

N.S. acknowledges support by the Italian Ministry of Economical Development (MISE) under the MISE DGISSEG-INGV 2020 project contract. This research was financially supported by the

"Copernicus Space Component – Sentinels rolling archive product user access, operations, maintenance and evolutions" project running at NOA/BEYOND, (contract No:4000116830/16/I-BG).

References

Ambraseys, N.N., and J. A. Jackson (1990). Seismicity and associated strain of central Greece between 1890 and 1988. *Geophys. J. Int.* **101**, 663–708.

Atzori, S., M. Manunta, G. Fornaro, A. Ganas, and S. Salvi (2008). The postseismic displacement of the 1999 Athens earthquake retrieved by DInSAR time series, *J. Geophys. Res.* **113**, B09309, https://doi.org/10.1029/2007JB005504.

Atzori, S., I. Hunstad, M. Chini, S. Salvi, C. Tolomei, C. Bignami, S. Stramondo, E. Trasatti, A. Antonioli, and E. Boschi (2009). Finite fault inversion of DInSAR coseismic displacement of the 2009 L'Aquila earthquake (central Italy), *Geophys. Res. Lett.* **36**, L15305.

Atzori, S., and A. Antonioli (2011). Optimal fault resolution in geodetic inversion of coseismic data, *Geophys. J. Int.* **185**, 529-538, https://doi.org/10.1111/j.1365-246X.2011.04955.x

Atzori, S., A. Antonioli, C. Tolomei, V. De Novellis, C. De Luca, F. Monterroso (2019). InSAR full-resolution analysis of the 2017–2018 M > 6 earthquakes in Mexico. *Remote Sens. Environ.* **234**, 111461, https://doi.org/10.1016/j.rse.2019.111461.

Caputo, R. (1990). Geological and structural study of the recent and active brittle deformation of the Neogene–Quaternary basins of Thessaly (Greece). Scientific Annals **12**. Aristotle University of Thessaloniki, Thessaloniki. 2 vols., 5 encl. 252 pp.

Caputo, R., and S. Pavlides (1993). Late Cainozoic geodynamic evolution of Thessaly and surroundings (central-northern Greece). *Tectonophysics* **223**, 339– 362.

Caputo, R. (1993). Morphotectonics and kinematics along the Tirnavos Fault, northern Larissa Plain, mainland Greece. Zeit. fur *Geomorph.* **94**, 167–185.

Caputo, R., J. P. Bravard, and B. Helly (1994). The Pliocene–Quaternary tecto-sedimentary evolution of the Larissa Plain (Eastern Thessaly, Greece). *Geodin. Acta* **7**, 57–85.

Caputo, R., B. Helly, S. Pavlides, and G. Papadopoulos (2004). Palaeoseismological investigation of the Tyrnavos Fault (Thessaly, Central Greece). *Tectonophysics* **394**. https://doi.org/10.1016/j.tecto.2004.07.047.

Caputo, R., B. Helly, S. Pavlides, and G. Papadopoulos (2006). Archaeo- and palaeoseismological investigations in Northern Thessaly (Greece): Insights for the seismic potential of the region. *Nat Hazards* **39**, 195–212, https://doi.org/10.1007/s11069-006-0023-9.

Caputo, R., A. Chatzipetros, S. Pavlides, and S. Sboras (2012). The Greek Database of Seismogenic Sources (GreDaSS): state-of-the-art for northern Greece. *Ann. Geophys.* **55**, 859–894. https://doi.org/10.4401/ag-5168.

Chatzipetros, A., I. Lazos, S. Pavlides, C. Pikridas, and S. Bitharis (2018). Determination of the active tectonic regime of Thessaly, Greece: a geodetic data based approach. XXI International Congress of the CBGA. Salzburg, 227.

Chatzipetros, A., S. Pavlides, M. Foumelis, S. Sboras, D. Galanakis, C. Pikridas, S. Bitharis, E. Kremastas, A. Chatziioannou, and I. Papaioannou (2021). The northern Thessaly strong earthquakes of March 3 and 4, 2021, and their neotectonic setting. *Bull. Geol. Soc. Greece* **58**, 222-255. doi:https://doi.org/10.12681/bgsg.27225.

Cheloni, D., and other 41 (2017), Geodetic model of the 2016 Central Italy earthquake sequence inferred from InSAR and GPS data, *Geoph. Res. Lett.* **44**, 6778-6787, https://doi.org/10.1002/2017GL073580.

Chousianitis, K., A. Ganas, and C. P. Evangelidis (2015). Strain and rotation rate patterns of mainland Greece from continuous GPS data and comparison between seismic and geodetic moment release. *J. Geophys. Res. Solid Earth* **120**, 3909–3931. https://doi.org/10.1002/2014JB011762.

Chousianitis, K., A. O. Konca, G. A. Tselentis, G. Papadopoulos, and M. Gianniou (2016). Slip model of the November 17, 2015 Mw = 6.5 Lefkada earthquake from the joint inversion of geodetic and seismic data. *Geophys. Res. Lett.* **43**, 7973–7981. https://doi.org/10.1002/2016GL069764.

Chousianitis, K., and A. O. Konca (2018). Coseismic slip distribution of the 12 June 2017 Mw = 6.3 Lesvos earthquake and imparted static stress changes to the neighboring crust. *J. Geophys. Res.* **123**, 8926– 8936, https://doi.org/10.1029/2018JB015950.

Chousianitis, K., and A. O. Konca (2019). Intraslab deformation and rupture of the entire subducting crust during the 25 October 2018 Mw 6.8 Zakynthos earthquake. *Geophys. Res. Lett.* **46**, 14358-14367. https://doi.org/10.1029/2019GL085845.

Chousianitis, K., X. Papanikolaou, G. Drakatos, and G. A. Tselentis (2021). NOANET: A Continuously Operating GNSS Network for Solid-Earth Sciences in Greece, *Seismol. Res. Lett.*, **92**, 2050–2064, https://doi.org/10.1785/0220200340.

Chousianitis, K., and A. O. Konca (2021). Rupture process of the 2020 Mw7.0 Samos earthquake and its effect on surrounding active faults. *Geophys. Res. Lett.* **48**, e2021GL094162, https://doi.org/10.1029/2021GL094162.

Constantini, M. (1998). A novel phase unwrapping method based on network programming. *IEEE Trans. Geosci. Remote Sens.* **36**, 813–821.

D'Agostino, N., M. Métois, R. Koci, L. Duni, N. Kuka, A. Ganas, I. Georgiev, F. Jouanne, N. Kaludjerovic, and R. Kandić (2020). Active crustal deformation and rotations in the southwestern Balkans from continuous GPS measurements. *Earth Planet. Sci. Lett.* **539**, https ://doi.org/10.1016/j.epsl.2020.116246.

De Novellis, V., D. Reale, G.M. Adinolfi, E. Sansosti, and V. Convertito (2021). Geodetic Model of the March 2021 Thessaly Seismic Sequence Inferred from Seismological and InSAR Data. *Remote Sens.* **13**, 3410. https://doi.org/10.3390/rs13173410.

Farr, T., G. and M. Kobrick (2000). Shuttle radar topography mission produces a wealth of data. *Eos Trans. AGU 2000* **81**, 583–585. https://doi.org/10.1029/EO081i048p00583.

Fotiou, A., C. Pikridas, D. Rossikopoulos, S. Spatalas, V. Tsioukas, and S. Katsougiannopoulos (2010). The Hermes GNSS NtripCaster of AUTh. *Bull Geodesy Geophys* **LXIX**, 35–43.

Galanakis, D., S. Sboras, G. Konstantopoulou, and M. Xenakis (2021). Neogene-Quaternary tectonic regime and macroseismic observations in the Tyrnavos-Elassona broader epicentral area of the March 2021, intense earthquake sequence. *Bull. Geol. Soc. Greece* **58**, 200-221. doi:https://doi.org/10.12681/bgsg.27196.

Ganas, A., G. Drakatos, S. Rontogianni, C. Tsimi, P. Petrou, M. Papanikolaou, P. Argyrakis, K. Boukouras, N. Melis, and G. Stavrakakis (2008). NOANET: the new permanent GPS network for Geodynamics in Greece, *Geophysical Research Abstracts* **10**, EGU2008-A-04380.

Ganas, A., S. Valkaniotis, V. Tsironi, I. Karasante, P. Elias, V. Kapetanidis, I. Kasssaras, G. Papathanassiou, and P. Briole (2021). The March 2021 seismic sequence in Larisa – Damasi, Thessaly (central Greece), its seismotectonic characteristics and geodynamic effects. Zenodo. http://doi.org/10.5281/zenodo.4617264.

Ganas, A., S. Valkaniotis, P. Briole, A. Serpetsidaki, V. Kapetanidis, I. Karasante, I. Kassaras, G. Papathanassiou, I. Karamitros, V. Tsironi, P. Elias, V. Sarhosis, A. Karakonstantis, E. Konstantakopoulou, P. Papadimitriou, and E. Sokos (2021). Domino-style earthquakes along blind normal faults in Northern Thessaly (Greece): kinematic evidence from field observations, seismology. SAR interferometry and GNSS. *Bull. Geol. Soc. Greece* **58**, 37. https://doi.org/10.12681/bgsg.27102.

Ganas, A., P. Elias, V. Kapetanidis, S. Valkaniotis, P. Briole, I. Kassaras, P. Argyrakis, A. Barberopoulou, and A. Moshou (2019). The July 20, 2017 M 6.6 Kos earthquake: seismic and geodetic evidence for an active north-dipping normal fault at the western end of the Gulf of Gökova (SE Aegean Sea), *Pure and Applied Geophysics* **176**, 4177–4211.

Goldstein, R., and C. Werner (1998). Radar Interferogram Phase Filtering for Geophysical Applications. *Geophys. Res. Lett.* **25,** 4035–4038.

Harris, R. A. (1998). Introduction to special section: Stress triggers, stress shadows, and implications for seismic hazard, *J. Geophys. Res.* **103**, 24,347–24,358.

Herring, T. A., R. W. King, M. A. Floyd, and S. C. McClusky (2018). Introduction to GAMIT-GLOBK Release 10.71. Cambridge: Massachusetts Institute of Technology.

Hodge, M., Å. Fagereng, and J. Biggs (2018). The role of coseismic Coulomb stress changes in shaping the hard link between normal fault segments. *Journal of Geophysical Research* **123**, 797–814. https://doi.org/10.1002/2017JB014927.

Kapetanidis, V., and I. Kassaras (2019). Contemporary crustal stress of the Greek region deduced from earthquake focal mechanisms. *J. Geodyn.* **123**, 55–82. https://doi.org/10.1016/j.jog.2018.11.004.

Karakostas, V.G., O. Tan, A. Kostoglou, E.E. Papadimitriou, and P. Bonatis (2021). Seismotectonic implications of the 2020 Samos, Greece, Mw7.0 mainshock based on high-resolution aftershock relocation and source slip model. *Acta Geophysica* **69**, 979–996.

Karakostas, V., C. Papazachos, E. Papadimitriou, M. Foumelis, A. Kiratzi, C. Pikridas, A. Kostoglou, C. Kkallas, N. Chatzis, S. Bitharis, A. Chatzipetros, A. Fotiou, C. Ventouzi, E. Karagianni, P. Bonatis, C. Kourouklas, P. Paradisopoulou, E. Scordilis, D. Vamvakaris, I. Grendas, D. Kementzetzidou, A. Panou, G. Karakaisis, I. Karagianni, P. Hatzidimitriou, and O. Galanis (2021). The March 2021 Tyrnavos, central Greece, doublet (Mw6.3 and Mw6.0): Aftershock relocation, faulting details, coseismic slip and deformation. *Bull. Geol. Soc. Greece* **58**, 131-178. https://doi.org/10.12681/bgsg.27237

Kassaras I., V. Kapetanidis, Ath. Ganas, A. Karakonstantis, P. Papadimitriou, G. Kaviris, V. Kouskouna, and N. Voulgaris (2022) Seismotectonic analysis of the 2021 Damasi-Tyrnavos (Thessaly, Central Greece) earthquake sequence and implications on the stress field rotations. *J. Geodyn* **150**, 101898, https://doi.org/10.1016/j.jog.2022.101898.

Kilias, A., C. Fasoulas, M. Priniotakis, A. Sfeikos, and W. Frisch (1991). Deformation and HP/LT Metamorphic Conditions at the Tectonic Window of Kranea (W – Thessaly, Northern Greece). Zeitschrift Der *Deutschen Geologischen Gesellschaft* **142**, 87–96. https://doi.org/10.1127/zdgg/142/1991/87.

Kilias, A., and D. Mountrakis (1987). Structural Geology of the Central Pelagonian Zone (Kamvounia Mountains, North Greece). Zeitschrift Der *Deutschen Geologischen Gesellschaft* **138**, 211–237. https://doi.org/10.1127/zdgg/138/1987/211.

Kiratzi, A., C. Papazachos, A. Özacar, A. Pinar, C. Kkallas, and E. Sopaci (2021). Characteristics of the 2020 Samos earthquake (Aegean Sea) using seismic data. Bull of Earthquake Eng, https://doi.org/10.1007/s10518-021-01239-1.

Konca, A. O., S. E. Guvercin, S. Ozarpaci, A. Ozdemir, G. Funning, U. Dogan, S. Ergintav, M. Floyd, H. Karabulut, and R. Reilinger (2019). Slip distribution of the 2017 Mw6.6 Bodrum–Kos earthquake: resolving the ambiguity of fault geometry, *Geophys. J. Int.* **219**, 911–923, https://doi.org/10.1093/gji/ggz332.

Koukouvelas, I.K., K.G. Nikolakopoulos, A. Kyriou, R. Caputo, A. Belesis, V. Zygouri, S. Verroios, D. Apostolopoulos, and I. Tsentzos (2021). The March 2021 Damasi Earthquake Sequence, Central Greece: Reactivation Evidence across the Westward Propagating Tyrnavos *Graben. Geosciences* **11**, 328. https://doi.org/10.3390/geosciences11080328.

Lazos, I., S. Sboras, K. Chousianitis, S. Bitharis, E. Mouzakiotis, V. Karastathis, C. Pikridas, A. Fotiou, and D. Galanakis (2021). Crustal deformation analysis of Thessaly (central Greece) before the March 2021 earthquake sequence near Elassona-Tyrnavos (northern Thessaly). *Acta Geodyn. Geomater.* **18**, 379-385, https://doi.org/10.13168/AGG.2021.0026

Lin, J., and R. S. Stein (2004). Stress triggering in thrust and subduction earthquakes and stress interaction between the southern San Andreas and nearby thrust and strike-slip faults. *J. Geophys. Res.* **109**, B02303. https://doi.org/10.1029/2003JB002607.

Massonnet, D., and K. L. Feigl (1995). Satellite radar interferometric map of the coseismic deformation field of the M = 6.1 Eureka Valley, California earthquake of May 17, 1993. *Geophys. Res. Lett.* **22**, 1541–1544.

Menke, W. (1989). Geophysical Data Analysis: Discrete Inverse Theory. 1st Edition, Academic Press, San Diego, 289.

Merryman Boncori, J.P., I. Papoutsis, G. Pezzo, C. Tolomei, S. Atzori, A. Ganas, V. Karastathis, S. Salvi, C. Kontoes, and A. Antonioli (2014). The February 2014 Cephalonia Earthquake (Greece): 3D Deformation Field and Source Modeling from Multiple SAR Techniques, *Seismol. Res. Lett.* **86**, 1, 124-137, January/February 2015. https://doi.org/10.1785/0220140126.

Okada, Y. (1985). Surface deformation due to shear and tensile faults in a half-space, *Bull. Seismol. Soc. Am.* **75**, 1135– 1154.

Papadopoulos, G.A., A. Ganas, A. Agalos, A. Papageorgiou, I. Triantafyllou, C. Kontoes, I. Papoutsis, and G. Diakogianni (2017). Earthquake Triggering Inferred from Rupture Histories, DInSAR Ground Deformation and Stress-Transfer Modelling: The Case of Central Italy During August 2016–January 2017. *Pure Appl. Geophys.* **174**, 3689–3711. https://doi.org/10.1007/s00024-017-1609-8.

Papadopoulos, G., A. Agalos, M. Charalampakis, C. Kontoes, I. Papoutsis, S. Atzori, N. Svigkas, and I. Triantafyllou (2019). Fault models for the Bodrum–Kos tsunamigenic earthquake (Mw6.6) of 20 July 2017 in the east Aegean Sea, *J. Geodyn.* **131**. https://doi.org/10.1016/j.jog.2019.101646.

Papadopoulos, G.A., A. Agalos, A. Karavias, I. Triantafyllou, I. Parcharidis, and E. Lekkas (2021). Seismic and Geodetic Imaging (DInSAR) Investigation of the March 2021 Strong Earthquake Sequence in Thessaly, Central Greece. *Geosciences* **11**, 311. https://doi.org/10.3390/geosciences11080311.

Papazachos, B.C., and C. Papazachou (1997). The Earthquakes of Greece. Editions ZITI, Thessaloniki. 304 pp.

Papoutsis, I., C. Kontoes, S. Alatza, A. Apostolakis, and C. Loupasakis (2020). InSAR Greece with Parallelized Persistent Scatterer Interferometry: A National Ground Motion Service for Big Copernicus Sentinel-1 Data, *Remote Sens.* **12**, 19, 3207. https://doi.org/10.3390/rs12193207.

Parsons, T., R. S. Stein, R. W. Simpson, and P. A. Reasenberg (1999). Stress sensitivity of fault seismicity: A comparison between limited-offset oblique and major strike-slip faults, *J. Geophys. Res.* **104**, 20,183–20,202.

Pavlides, S., and S. Sboras (2021). Recent earthquake activity of March 2021 in northern Thessaly unlocks new scepticism on Faults. *Turkish J Earth Sci* **30,** 1-11. https://doi.org/10.3906/yer-2110-6.

Pavlides S., A. Chatzipetros, S. Sboras, E. Kremastas, and A. Chatziioannou (2021). The northern Thessaly strong earthquakes of March 3 and 4 and their neotectonic setting. Earthquake Geology Research Team, Thessaloniki, Greece. https://doi.org/10.5281/zenodo.4618188.

Sboras, S. (2011). The Greek Database of Seismogenic Sources: seismotectonic implications for North Greece. PhD thesis, University of Ferrara.

Sboras, S., S. Pavlides, R. Caputo, A. Chatzipetros, A. Michailidou, S. Valkaniotis, and G. Papathanassiou (2014). The use of geological data to improve SHA estimates in Greece. *Bollettino Di Geofisica Teorica Ed Applicata* **55**. https://doi.org/10.4430/bgta0101.

Sboras, S., I. Lazos, E. Mouzakiotis, V. Karastathis, S. Pavlides, and A. Chatzipetros (2020). Fault modelling, seismic sequence evolution and stress transfer scenarios for the July 20, 2017 (MW 6.6) Kos–Gökova Gulf earthquake, SE Aegean. *Acta Geophysica* **68**, 1245–1261, https://doi.org/10.1007/s11600-020-00471-8.

Sykioti, O., C. Kontoes, P. Elias, P. Briole, M. Sachpazi, D. Paradissis, and I. Kotsis (2003). Ground deformation at Nisyros volcano (Greece) detected by ERS-2 SAR differential interferometry. *Int. J. Remote Sens.* **24**, 183-188, https://doi.org/10.1080/01431160305000.

Svigkas, N., S. Atzori, A. Kiratzi, C. Tolomei, A. Antonioli, I. Papoutsis, S. Salvi, and Ch. Kontoes (2019). On the Segmentation of the Cephalonia–Lefkada Transform Fault Zone (Greece) from an InSAR Multi-Mode Dataset of the Lefkada 2015 Sequence, *Remote Sens.* **11**, 16, 1848. https://doi.org/10.3390/rs11161848.

Toda, S., R. S. Stein, K. Richards-Dinger, and S. B. Bozkurt (2005). Forecasting the evolution of seismicity in southern California: Animations built on earthquake stress transfer. *J. Geophys. Res.* **110**, B05S16. https://doi.org/10.1029/2004JB003415.

Valkaniotis S., G. Papathanassiou, Ath. Ganas, E. Kremastas, and R. Caputo (2021). Preliminary report of liquefaction phenomena triggered by the March 2021 earthquakes in Central Thessaly, Greece. Report, Zenodo repository: https://doi.org/10.5281/zenodo.4608365.

Williams, C. A., and G. Wadge (1998). The effects of topography on magma chamber deformation models: Application to Mt. Etna and radar interferometry, *Geophys. Res. Lett.* **25**, 10, 1549–1552. https://doi.org/10.1029/98GL01136.

Wright, T. J., Z. Lu, and C. Wicks (2003). Source model for the Mw 6.7, 23 October 2002, Nenana Mountain Earthquake (Alaska) from InSAR, *Geophys. Res. Lett.* **30**, 18, 1974. https://doi.org/10.1029/2003GL018014.

Full mailing addresses for each author

[1] Institute for Astronomy, Astrophysics, Space Applications and Remote Sensing, Center for Earth Observation Research and Satellite Remote Sensing BEYOND, National Observatory of Athens, Metaxa & Vas. Pavlou, 15236, Athens, Greece

[2] Institute of Geodynamics, National Observatory of Athens, Lofos Nymfon, 11810, Athens, Greece

[3] Instituto Nazionale di Geofisica e Vulcanologia, 00143 Rome, Italy

[4] Laboratory of Engineering Geology and Hydrogeology, Department of Geological Sciences, School of Mining and Metallurgical Engineering, National Technical University of Athens, 15780 Athens, Greece

C. Kontoes[1] : kontoes@noa.gr

S. Alatza[1] : alatza@noa.gr

K. Chousianitis[2] : chousianitis@noa.gr

N. Svigkas[3] : nikos.svigkas@ingv.it

C. Loupasakis[4] : cloupasakis@metal.ntua.gr

S. Atzori[3] : simone.atzori@ingv.it

A. Apostolakis[1] : alex.apostolakis@noa.gr

Table 1. Coseismic static offsets of the M_w 6.3 and M_w 6.0 earthquakes from low-rate (30 s) GPS data and associated uncertainties. Boxes without reported values denote components where the estimated offsets were zero.

			M_w 6.3 earthquake offsets (3 March 10:16:08)		
Station	**Long. (°)**	**Lat. (°)**	**N-S (cm)**	**E-W (cm)**	**Up (cm)**
LARI	22.388	39.614	0.355±0.22	-	-
ELAS	22.206	39.892	2.981±0.25	1.156±0.20	0.856±0.82
KLOK	22.014	39.565	-2.792±0.22	-2.498±0.19	-
KRDI	21.923	39.366	-0.624±0.21	-0.460±0.20	-
			M_w 6.0 earthquake offsets (4 March 18:38:19)		
LARI	22.388	39.614	-	-	-
ELAS	22.206	39.892	1.345±0.24	0.781±0.21	0.668±0.85
KLOK	22.014	39.565	-1.006±0.21	-0.372±0.19	-
KRDI	21.923	39.366	-0.273±0.19	-0.148±0.19	-

Table 2. Best-fit parameters (1-σ uncertainty within brackets) after non-linear inversion of the three sources. Both nodal planes are reported for the third event.

Event	Length (km)	Width (km)	Depth[a] (km)	Lon (°)	Lat (°)	Strike (°)	Dip (°)	Rake (°)	Slip (m)	Moment (N·m)
M_w 6.3	11.1 (0.5)	9.4 (0.7)	1.4 (0.2)	22.165 (0.002)	39.687 (0.002)	312.2 (1.7)	39.6 (4.6)	-90.1 (11.6)	0.82 (0.04)	$2.93\cdot10^{18}$
M_w6.0	9.9 (0.9)	5.0[b]	3.3 (0.6)	22.069 (0.008)	39.771 (0.008)	289.5 (7.3)	43.1 (9.3)	-107.8 (11.9)	0.50 (0.09)	$7.4\cdot10^{17}$
M_w 5.2[c] NE dip	4.3 (0.5)	3.0[b]	3.1 (0.3)	21.995 (0.002)	39.826 (0.002)	286.5 (9.5)	29.2 (3.4)	-87.4 (10.1)	0.51 (0.08)	$2.0\cdot10^{17}$
M_w 5.2 SW dip	4.4 (0.4)	3.1 (0.7)	2.8 (0.2)	21.995 (0.003)	39.820 (0.002)	106.5 (5.3)	54.0 (4.2)	-87.1 (10.0)	0.50 (0.08)	$2.0\cdot10^{17}$

(a) Vertical depth of the fault top edge, (b) constrained a priori, (c) preferred solution

Table 3. GPS data used in the inversion of the M_w 6.3 and M_w 6.0 seismic events. Observed values contain the cumulated effects of the M_w 6.3 and M_w 6.0 earthquakes. Boxes without reported values denote components where the estimated offsets were zero.

			Observed (cm)			Modeled (cm)		
SITE	Lon (°)	Lat (°)	East	North	Up	East	North	Up
ELAS	22.2061	39.8924	1.93	4.32	1.524	1.51	2.92	0.4618
KLOK	22.0143	39.5647	-2.87	-3.79	-	-3	-3.55	0.1653
KRDI	21.9226	39.3664	-0.6	-0.89	-	-0.61	-0.95	-0.069
LARI	22.38791	39.61411	-	0.355	-	0.1074	0.3887	0.4078

List of Figure Captions

Figure 1. Geographical and tectonic setting of Thessaly plain. (a) Seismicity in Thessaly plain from 3 March 2021 until November 2021. Red stars denote the locations of the mainshocks (M_w 6.3, M_w 6.0, M_w 5.2). Larissa (LF), Tyrnavos (TF), Rodia (RF) and Ligaria (IF) faults, are added according to Caputo et al. (2004). Colored circles represent all the seismic events of March 2021, that occurred in the study area (epicenters are from http://bbnet.gein.noa.gr). (b) Footprints of Sentinel-1 satellite tracks, used to produce the co-seismic interferograms. The area of interest is depicted with the red rectangle. (c) Locations of GPS stations and GPS offsets of the M_w 6.3 and M_w 6.0 seismic events. Focal mechanisms are from this study.

Figure 2. Sentinel-1 SAR interferometric products corresponding to the sequence of Thessaly earthquakes. In the coseismic interferograms each fringe indicates a ground deformation of 2.8 cm. (a) Interferogram from ascending track 102, depicting the M_w 6.3 earthquake of 3 March, 2021 (b) Interferogram from ascending track 102 showing the deformation pattern resulted from the M_w 6.0 earthquake of 4 March, 2021) (c) Interferogram from ascending track 175 illustrating the deformation field caused by the M_w 5.2 earthquake of 12 March 2021 (d) Displacement map calculated from descending track 80, as induced by the three investigating earthquake events together. (e) Interferogram from descending track 80 showing the surface deformation pattern from all three seismic events. The corresponding seismic sources (black rectangles), are also illustrated. Red stars denote the locations of the earthquake epicenters. Larissa (LF), Tyrnavos (TF), Rodia (RF) and Ligaria (IF) faults, are added according to Caputo et al. (2004).

Figure 3. Daily position time series of the GPS stations that captured the static coseismic effects of the M_w 6.3 (3 March 2021, 10:16:08), the M_w 6.0 (4 March 2021, 18:38:19) and the M_w 5.2 (12 March 2021,

12:57:50) earthquakes. The error bars represent 1-σ uncertainties. Vertical dashed lines labeled with (1), (2) and (3) indicate the occurrences of the M_w 6.3, M_w 6.0 and M_w 5.2 earthquakes, respectively.

Figure 4. Comparison between observed and modeled InSAR Line-of-sight (LoS) displacement data and residuals, with *ad hoc* legend, for the ascending and descending orbits and including the M_w 6.3 and M_w 6.0 earthquakes. Local residuals are still present, due to liquefaction or local fluctuations from the planar elastic model.

Figure 5. Comparison between observed and modeled InSAR Line-of-sight (LoS) displacement data and residuals, for the ascending and descending orbits, of the M_w 5.2 earthquake.

Figure 6. 3D "cloud of solutions" for the three events (only the NE dipping plane for M_w 5.2) after the statistical analysis, with 50 different sources (for each event) obtained by non-linearly inverting InSAR data perturbed with ad hoc noise. It gives a qualitative idea of the robustness of the best-fit solutions (black rectangles) and supports the hypothesis that the first two events occurred on the same fault system.

Figure 7. Slip model distributions, in geographic and frontal views, for the mainshock and the two aftershocks. The third source solutions for the two fault planes (see Table 2) are reported in black for the preferred option (NE dipping) and gray for the alternative solution (SW dipping). The slip distribution is provided for both options in the frontal view and only for the preferred option (NE dipping) in the map. The same scale bar applies to all the slip distributions. Fault patches are 1 x 1 km; slip distributions are completed with the vertical depths and focal mechanisms (ellipses describe 1-sigma uncertainty). Black dashed lines indicate the trace of the modeled fault (in gray the SW dipping plane for the third event) and black rectangles the uniform slip solutions from non-linear inversion. Larissa (LF), Tyrnavos (TF), Rodia (RF) and Ligaria (IF) faults are added according to Caputo et al. (2004). Stars indicate the event epicenters.

Figure 8. Maximum Coulomb stress changes on optimally oriented normal faults over the depth ranges that are reported on the top right of each panel. a) Stresses imparted by the M_w 6.3 earthquake based on its slip distribution. Superimposed are the aftershocks with M_L>2.0 which occurred in the time interval between the M_w 6.3 earthquake of 3 March and the M_w 6.0 earthquake of 4 March. The latter is denoted as a green star and is depicted in two depth ranges in order to account for uncertainty in the hypocenter estimation which according to the NOA catalog is 8 km. Green beach ball represents the fault plane solution of the M_w 6.0 earthquake. Black circle denotes the area where no aftershocks occurred prior to the occurrence of the M_w 6.0 rupture. Yellow star denotes the M_w 6.3 earthquake of 3 March, which is depicted in two depth ranges for the same reason as for the M_w 6.0 earthquake. b) Stresses imparted by the M_w 6.3 and M_w 6.0 earthquakes. The depicted seismicity (M_L>2.0) corresponds to the aftershock sequence until the occurrence of the M_w 5.2 earthquake of 12 March which is denoted as a green star. The latter is shown in two depth ranges so as to account for uncertainty in the hypocenter estimation which according to the NOA catalog is 7 km. Green beach ball represents the fault plane solution of the M_w 5.2 earthquake. c) Stresses imparted by the M_w 6.3, M_w 6.0 and M_w 5.2 earthquakes. Superimposed are the seismic events with M_L>2.0 which occurred after the origin time of the M_w 5.2 earthquake of 12 March and until November 2021. Fault abbreviations are: Larissa (LF), Tyrnavos (TF), Rodia (RF) and Ligaria (IF).

Figure 9. Coulomb stress changes transferred by the M_w 6.3, M_w 6.0 and M_w 5.2 ruptures to surrounding major active faults. The results stay the same irrespectively of whether we use the slip distribution of the NE- or the SW-dipping fault plane for the M_w 5.2 event. Fault abbreviations are: Larissa (LF), Tyrnavos (TF) and Rodia (RF). Solid red lines indicate the surface trace of the aforementioned faults. Green stars and corresponding beach balls indicate the epicenters and fault plane solutions of the M_w 6.0 and M_w 5.2 earthquakes.

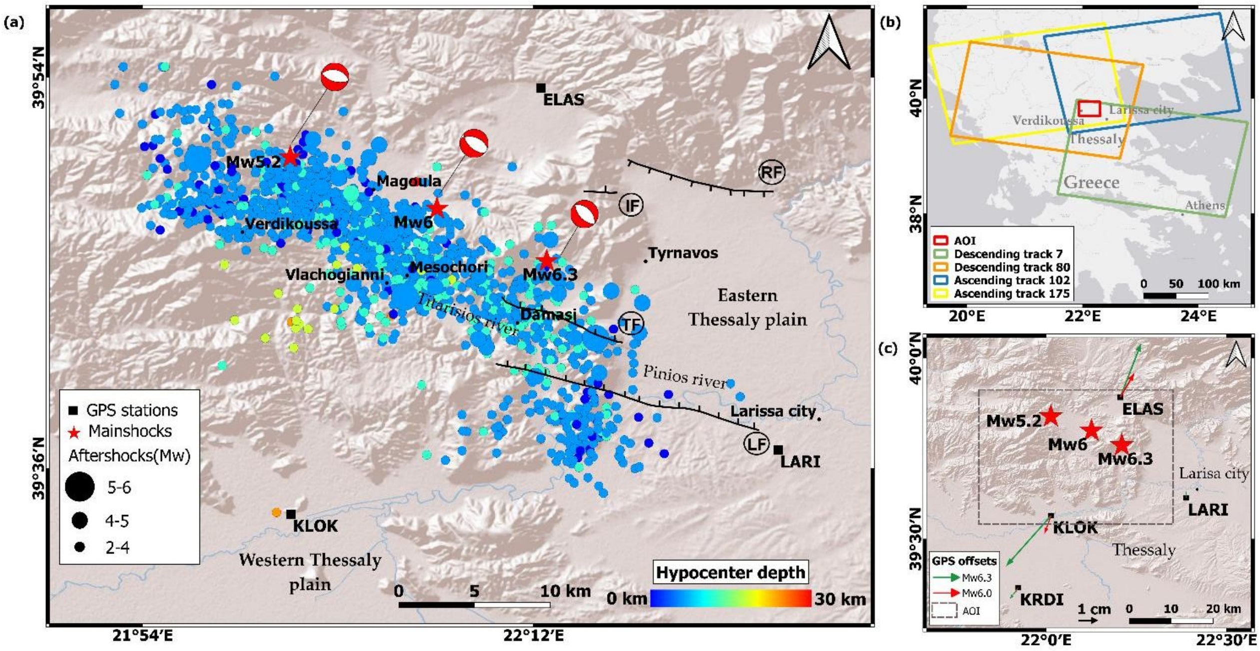

Figure 1. Geographical and tectonic setting of Thessaly plain. (a) Seismicity in Thessaly plain from 3 March 2021 until November 2021. Red stars denote the locations of the mainshocks (M_w 6.3, M_w 6.0, M_w 5.2). Larissa (LF), Tyrnavos (TF), Rodia (RF) and Ligaria (IF) faults, are added according to Caputo et al. (2004). Colored circles represent all the seismic events of March 2021, that occurred in the study area (epicenters from http://bbnet.gein.noa.gr). (b) Footprints of Sentinel-1 satellite tracks, used to produce the co-seismic interferograms. The area of interest is depicted with a red rectangle. (c) Locations of GPS stations and GPS offsets of the M_w 6.3 and M_w 6.0 seismic events. Focal mechanisms are from this study.

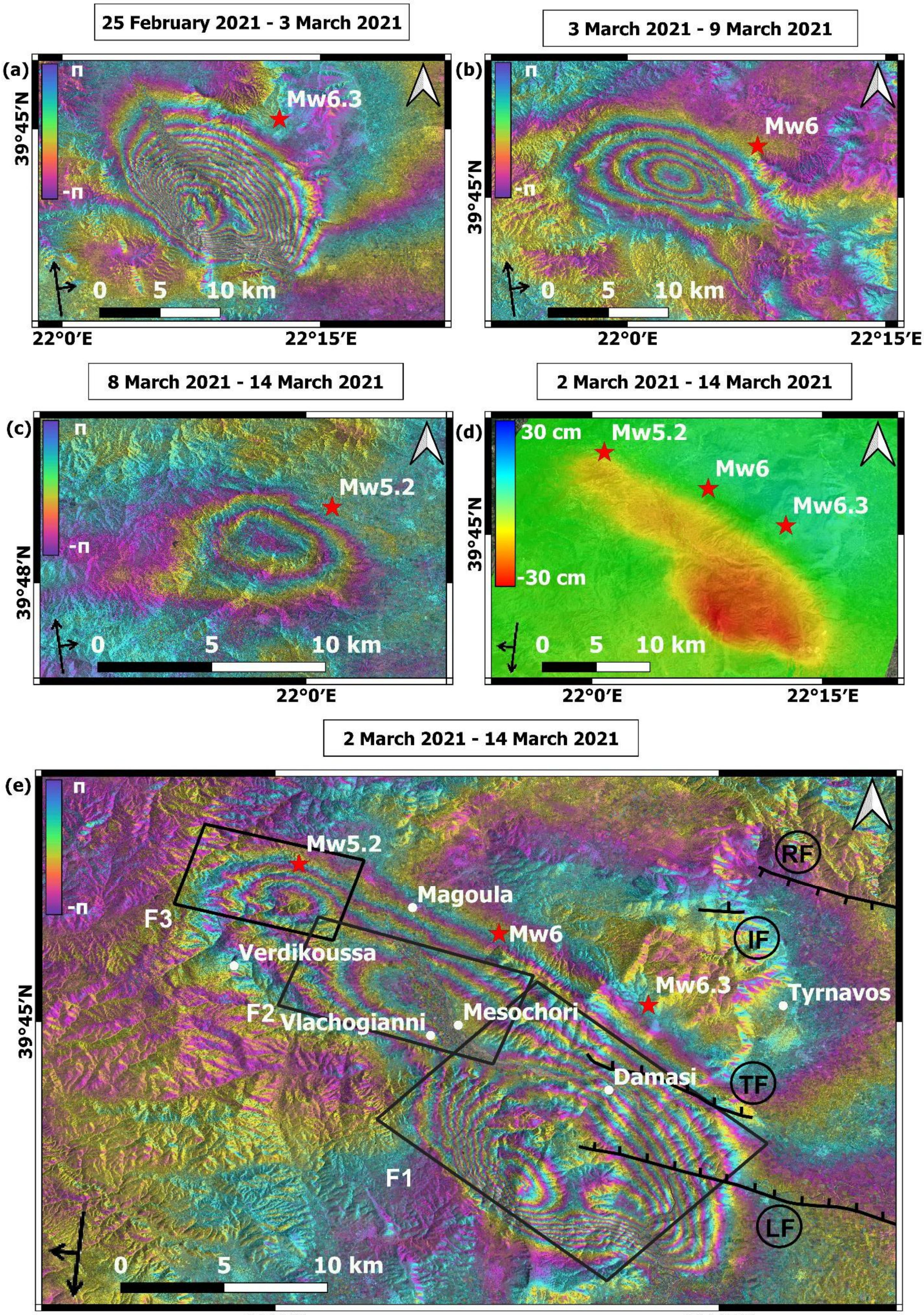

25 February 2021 - 3 March 2021
(a)
π
-π
Mw6.3
39°45′N
0
5
10 km
22°0′E
22°15′E
3 March 2021 - 9 March 2021
(b)
π
-π
Mw6
39°45′N
0
5
10 km
22°0′E
22°15′E
8 March 2021 - 14 March 2021
(c)
π
-π
Mw5.2
39°48′N
0
5
10 km
22°0′E
2 March 2021 - 14 March 2021
(d)
30 cm
-30 cm
Mw5.2
Mw6
Mw6.3
39°45′N
0
5
10 km
22°0′E
22°15′E
2 March 2021 - 14 March 2021
(e)
π
-π
Mw5.2
Magoula
F3
Mw6
Verdikoussa
Mw6.3
Tyrnavos
F2
Vlachogianni
Mesochori
Damasi
F1
RF
IF
TF
LF
39°45′N
0
5
10 km
22°0′E
22°15′E

Figure 2. Sentinel-1 SAR interferometric products corresponding to the sequence of Thessaly earthquakes. In the coseismic interferograms each fringe indicates a ground deformation of 2.8 cm. (a) Interferogram from ascending track 102, depicting the M_w 6.3 earthquake of 3 March, 2021 (b) Interferogram from ascending track 102 showing the deformation pattern resulted from the M_w 6.0 earthquake of 4 March, 2021) (c) Interferogram from ascending track 175 illustrating the deformation field caused by the M_w 5.2 earthquake of 12 March 2021 (d) Displacement map calculated from descending track 80, as induced by the three investigating earthquake events together. (e) Interferogram from descending track 80 showing the surface deformation pattern from all three seismic events. The corresponding seismic sources (black rectangles), are also illustrated. Red stars denote the locations of the earthquake epicenters. Larissa (LF), Tyrnavos (TF), Rodia (RF) and Ligaria (IF) faults, are added according to Caputo et al. (2004).

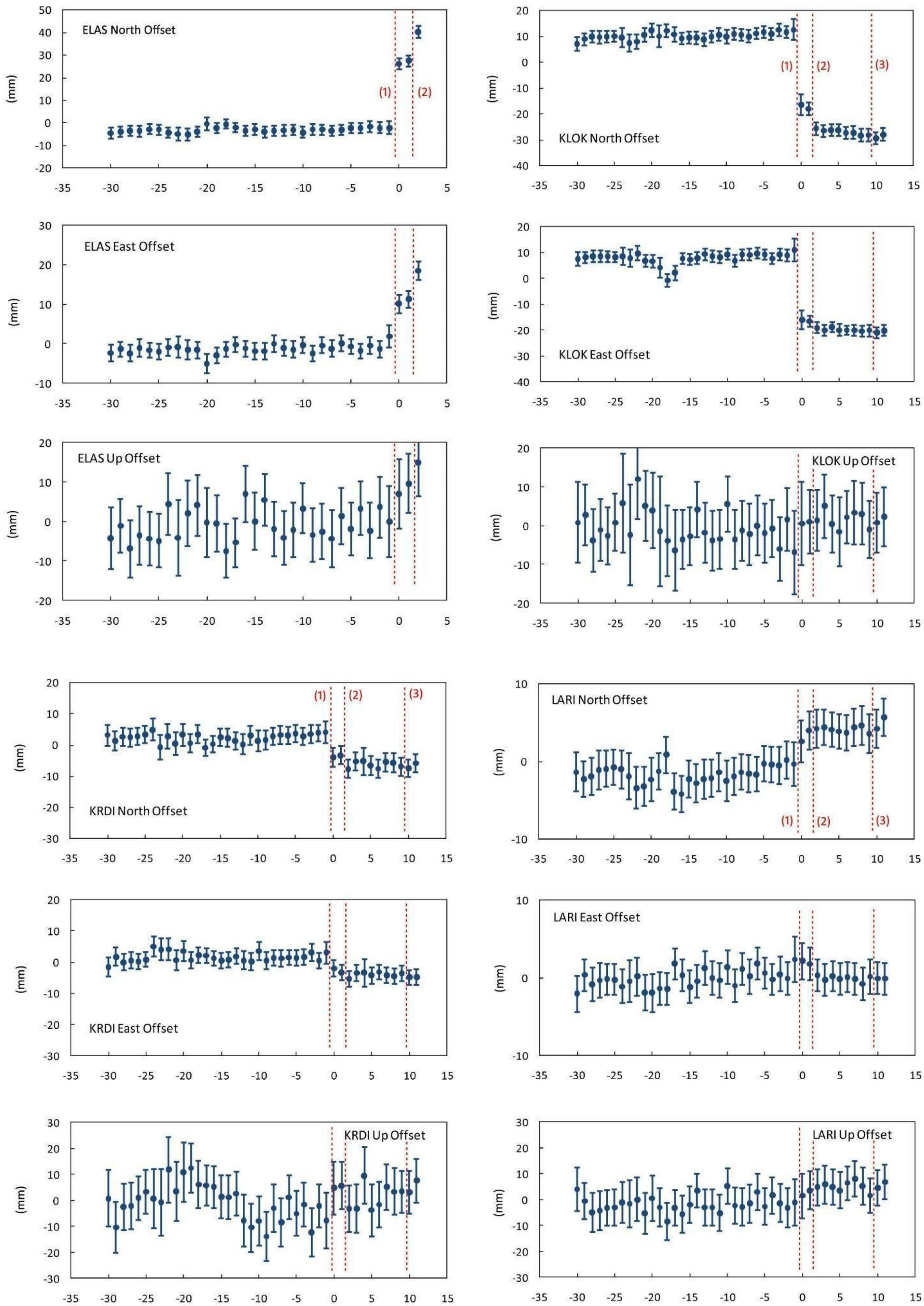
ELAS North Offset
ELAS East Offset
ELAS Up Offset
KLOK North Offset
KLOK East Offset
KLOK Up Offset
KRDI North Offset
KRDI East Offset
KRDI Up Offset
LARI North Offset
LARI East Offset
LARI Up Offset
(mm)
(1)
(2)
(3)

Figure 3. Daily position time series of the GPS stations that captured the static coseismic effects of the M_w 6.3 (3 March 2021, 10:16:08), the M_w 6.0 (4 March 2021, 18:38:19) and the M_w 5.2 (12 March 2021, 12:57:50) earthquakes. The error bars represent 1-σ uncertainties. Vertical dashed lines labeled with (1), (2) and (3) indicate the occurrences of the M_w 6.3, M_w 6.0 and M_w 5.2 earthquakes, respectively.

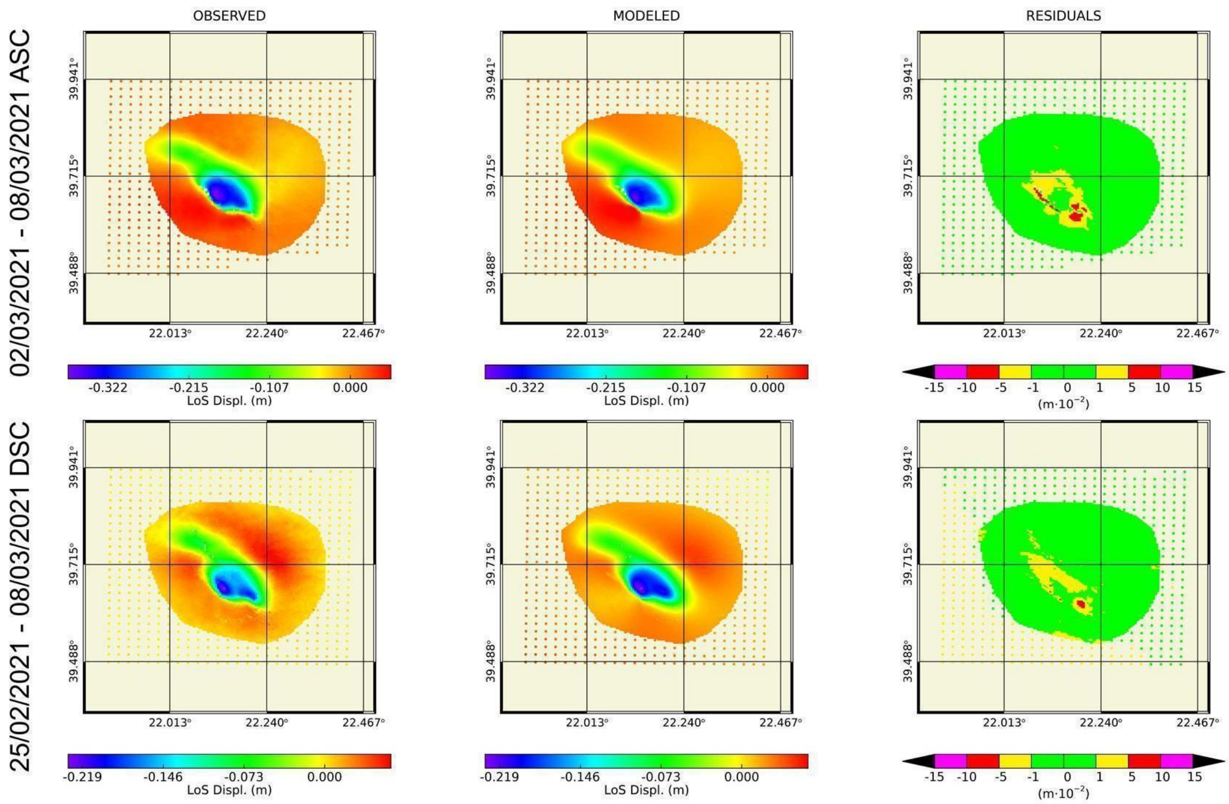

Figure 4. Comparison between observed and modeled InSAR Line-of-sight (LoS) displacement data and residuals, with *ad hoc* legend, for the ascending and descending orbits and including the M_w 6.3 and M_w 6.0 earthquakes. Local residuals are still present, due to liquefaction or local fluctuations from the planar elastic model.

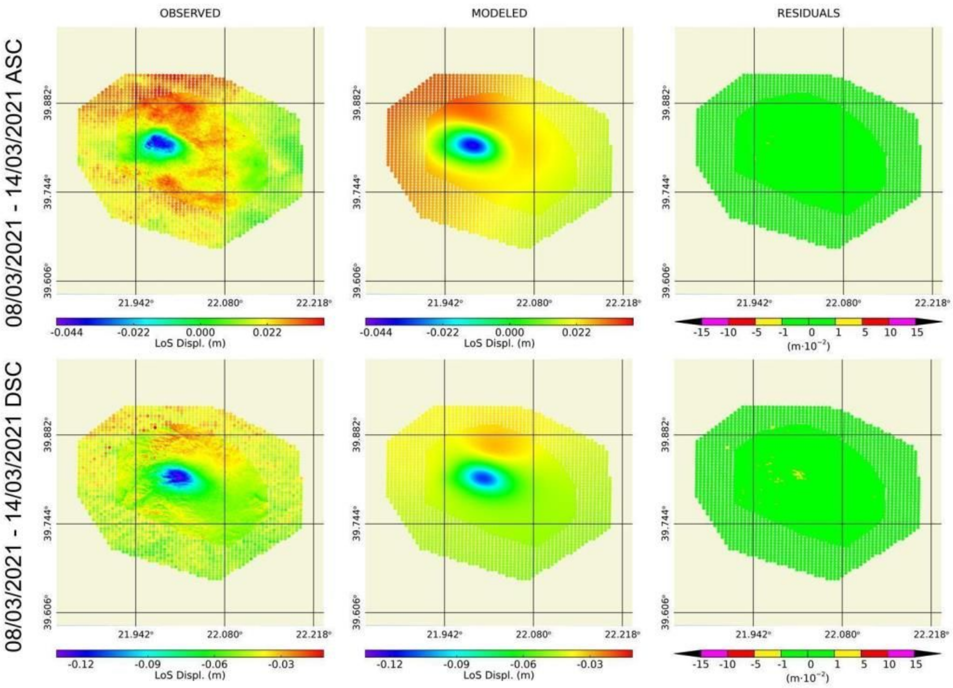

Figure 5. Comparison between observed and modeled InSAR Line-of-sight (LoS) displacement data and residuals, for the ascending and descending orbits, of the M_w 5.2 earthquake.

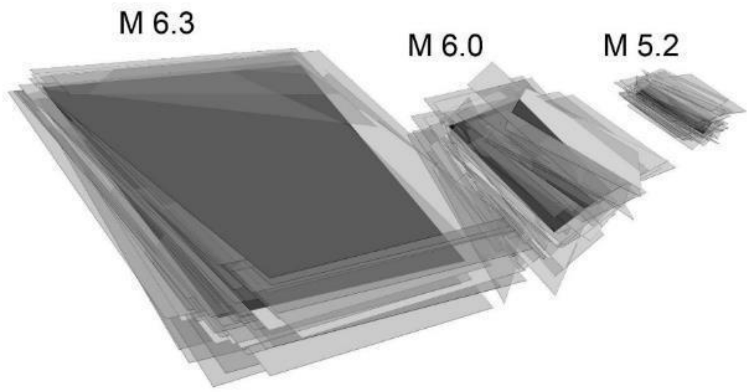

Figure 6. 3D "cloud of solutions" for the three events (only the NE dipping plane for M_w 5.2) after the statistical analysis, with 50 different sources (for each event) obtained by non-linearly inverting InSAR

data perturbed with ad *hoc noise*. It gives a qualitative idea of the robustness of the best-fit solutions (black rectangles) and supports the hypothesis that the first two events occurred on the same fault system.

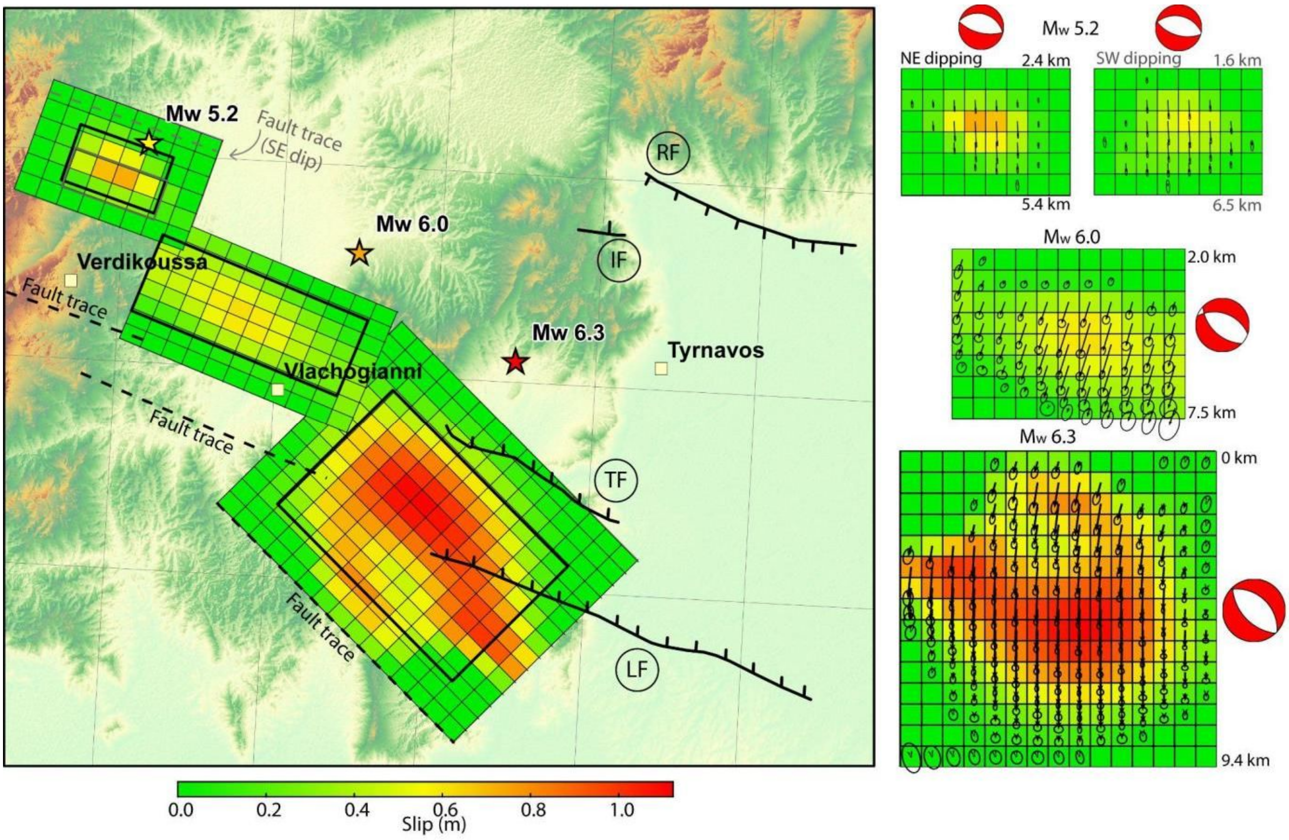

Figure 7. Slip model distributions, in geographic and frontal views, for the mainshock and the two aftershocks. The third source solutions for the two fault planes (see Table 2) are reported in black for the preferred option (NE dipping) and gray for the alternative solution (SW dipping). The slip distribution is provided for both options in the frontal view and only for the preferred option (NE dipping) in the map. The same scale bar applies to all the slip distributions. Fault patches are 1 x 1 km; slip distributions are completed with the vertical depths and focal mechanisms (ellipses describe 1-sigma uncertainty). Black dashed lines indicate the trace of the modeled fault (in gray the SW dipping plane for the third event) and black rectangles the uniform slip solutions from non-linear inversion. Larissa (LF), Tyrnavos (TF),

Rodia (RF) and Ligaria (IF) faults are added according to Caputo et al. (2004). Stars indicate the event epicenters.

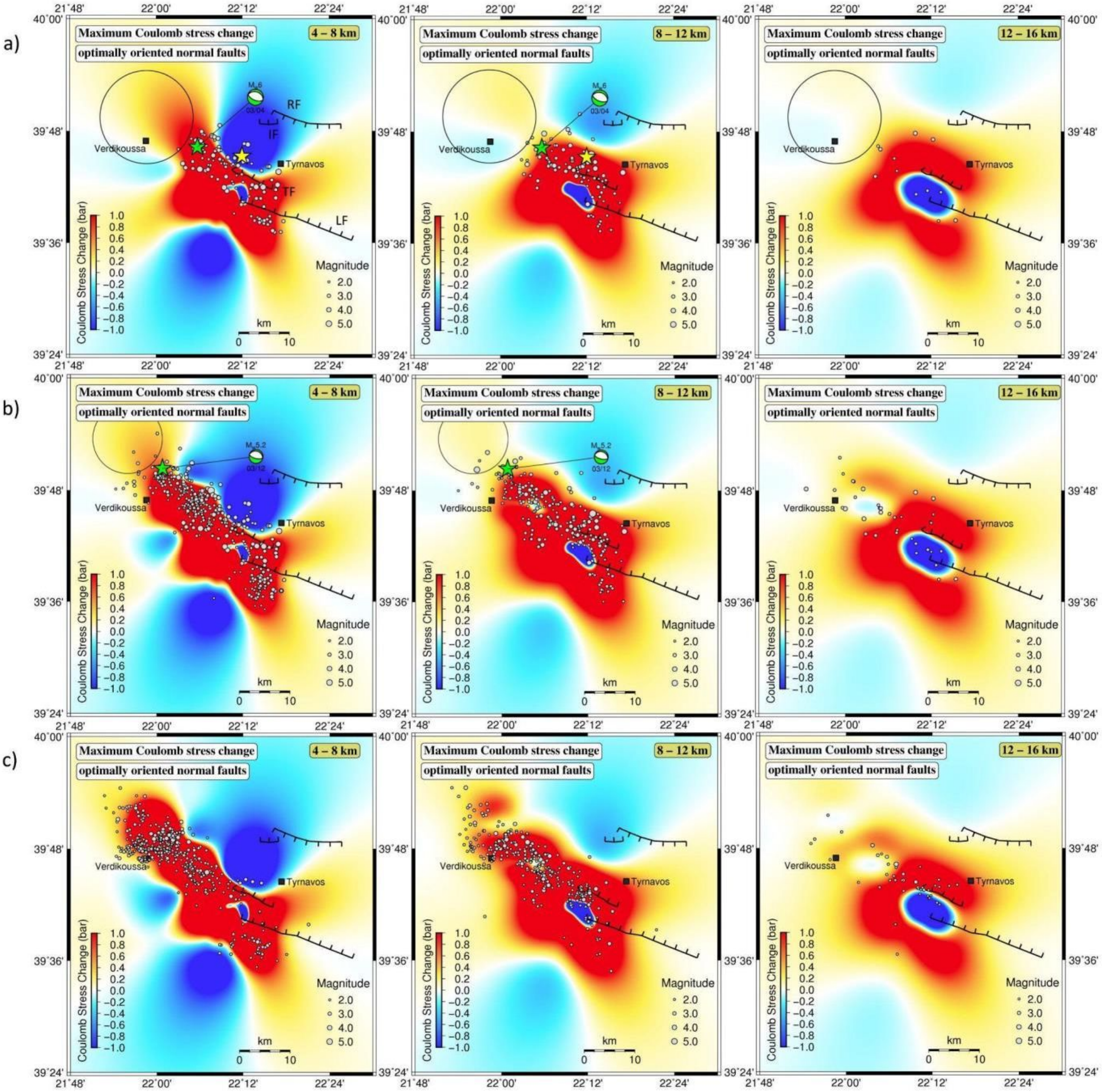

Figure 8. Maximum Coulomb stress changes on optimally oriented normal faults over the depth ranges that are reported on the top right of each panel. a) Stresses imparted by the M_w 6.3 earthquake based on its slip distribution. Superimposed are the aftershocks with M_L>2.0 which occurred in the time interval between the M_w 6.3 earthquake of 3 March and the M_w 6.0 earthquake of 4 March. The latter is denoted as a green star and is depicted in two depth ranges in order to account for uncertainty in the hypocenter

estimation which according to the NOA catalog is 8 km. Green beach ball represents the fault plane solution of the M_w 6.0 earthquake. Black circle denotes the area where no aftershocks occurred prior to the occurrence of the M_w 6.0 rupture. Yellow star denotes the M_w 6.3 earthquake of 3 March, which is depicted in two depth ranges for the same reason as for the M_w 6.0 earthquake. b) Stresses imparted by the M_w 6.3 and M_w 6.0 earthquakes. The depicted seismicity (M_L>2.0) corresponds to the aftershock sequence until the occurrence of the M_w 5.2 earthquake of 12 March which is denoted as a green star. The latter is shown in two depth ranges so as to account for uncertainty in the hypocenter estimation which according to the NOA catalog is 7 km. Green beach ball represents the fault plane solution of the M_w 5.2 earthquake. c) Stresses imparted by the M_w 6.3, M_w 6.0 and M_w 5.2 earthquakes. Superimposed are the seismic events with M_L>2.0 which occurred after the origin time of the M_w 5.2 earthquake of 12 March and until November 2021. Fault abbreviations are: Larissa (LF), Tyrnavos (TF), Rodia (RF) and Ligaria (IF).

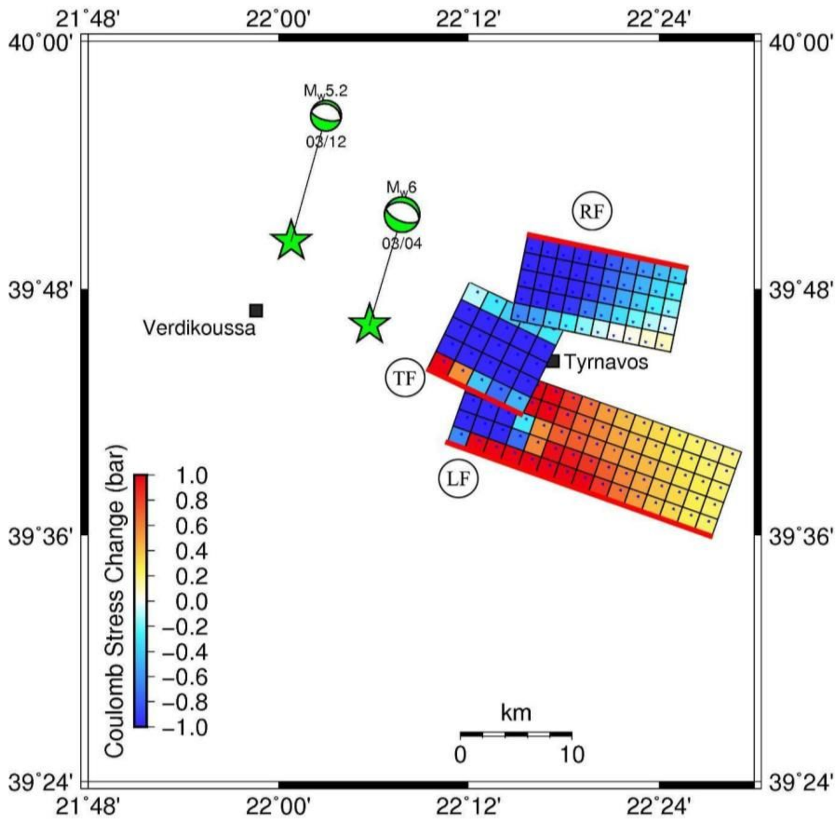

Figure 9. Coulomb stress changes transferred by the M_w 6.3, M_w 6.0 and M_w 5.2 ruptures to surrounding major active faults. The results stay the same irrespectively of whether we use the slip distribution of the NE- or the SW-dipping fault plane for the M_w 5.2 event. Fault abbreviations are: Larissa (LF), Tyrnavos (TF) and Rodia (RF). Solid red lines indicate the surface trace of the aforementioned faults. Green stars and corresponding beach balls indicate the epicenters and fault plane solutions of the M_w 6.0 and M_w 5.2 earthquakes.